Slip Localization Behavior at Triple Junctions in Nickel-Base Superalloys

Jonathan M. Hestroffer[1,a], Jean-Charles Stinville[b], Marie-Agathe Charpagne[b], Matthew P. Miller[c], Tresa M. Pollock[a], Irene J. Beyerlein[a,d]

[a] *Materials Department, University of California, Santa Barbara, CA, USA*
[b] *University of Illinois at Urbana-Champaign, Urbana, USA*
[c] *Mechanical and Aerospace Engineering, Cornell University, Ithaca, NY USA*
[d] *Department of Mechanical Engineering, University of California, Santa Barbara Santa Barbara, CA, USA*

Abstract

Incipient slip localization in the vicinity of hundreds of grain boundary triple junctions (TJs) in a lightly deformed nickel-base superalloy IN718 is studied using a combination of three-dimensional (3D) crystal plasticity finite element (CPFE) modeling, high resolution digital image correlation (HR-DIC) and 3D electron back-scatter diffraction tomography (3D EBSD). A 3D reconstruction method enables identification of thousands of TJs and correspondence of any observed slip bands with their originating TJ lines below the specimen surface. We present a large-scale CPFE model of the experimental 3D microstructure composed of high-fidelity representation of the TJ lines and the boundaries and interiors of the parent grains and use it to calculate the local micromechanical response and slip activity of all TJs at the onset of macroscopic yielding. Statistical analysis of the calculated quantities reveal TJs develop larger stress concentration and grain-average re-orientation than grain interiors and grain boundaries, however no substantial differences in cumulative slip were found among these microstructural regions. We find that TJs with observed slip bands generate lower grain-average re-orientation, fewer active slip systems, and more localized slip on a single system than those without. The distinctions in the reorientation and slip activity are stronger in TJs that experience more intense slip.

Keywords: Strain Localization, Superalloys, Microstructure, Crystal Plasticity Finite Element

1. Introduction

Polycrystalline nickel-base superalloys are most commonly used for turbine disk applications in gas turbine engines due to their exceptional strength, as well as oxidation and corrosion resistance at high temperatures [1]. Fatigue resistance is another critical property of these alloys as turbine disk components experience significant fluctuations in stress due to repeated take-off landing cycles. With minimal metallurgical defect content, the initiation of fatigue microcracks in these alloys is correlated with microstructure and tied to subgrain strain localization processes [2, 3]. In highly engineered, defect-free polycrystalline nickel-base superalloys, plastic strain localizes in the form of slip

---

[*] corresponding author: jonathanhestroffer@ucsb.edu

Email address: `jonathanhestroffer@ucsb.edu` (Jonathan M. Hestroffer) bands [4]. While many bands form throughout the microstructure, those which undergo the most intense slip displacements are of special interest as they are shown to further accumulate slip during cycling, leading to the initiation of fatigue microcracks [5–7]. These most problematic bands are also found to form during the first application of load, making the study of incipient plasticity in these materials of great interest [6, 8]. Recent experimental studies conducted on these alloys have revealed that critically intense bands are likely to form adjacent to triple junctions (TJs) (i.e. the one-dimensional intersection of three grain boundaries), and particular twin boundaries. However much less is understood about the subgrain micromechanics that promote slip band formation in these areas [6, 7, 9, 10].

Most knowledge of slip band formation in polycrystalline nickel-base superalloys comes from slip trace analysis, usually through a combination of high resolution imaging and electron back scatter diffraction (EBSD). Combining with discontinuity tolerant codes, like Heaviside-DIC (H-DIC), additionally allows for quantification of slip localization on the level of individual slip systems. However, because they are surface techniques, information on where slip bands originate is limited. Recent advances in experiments and multi-modal data merging tools have since enabled location of where surface visible bands in these alloys emanate beneath the specimen surface. Recently, Charpagne et al. [10] combined HR-DIC and three dimensional electron back-scatter diffraction tomography (3D EBSD) to reconstruct the planes for a large number of slip bands in nickel-base superalloy Inconel 718 (IN718) after monotonic deformation. The analysis revealed that over half of the slip bands visible at the surface are connected to grain boundary TJ lines located below the surface. Statistical analyses of hundreds of slip bands revealed the most intense bands were those associated with subsurface TJ lines and those simultaneously formed parallel and close to annealing twin boundaries. These results established the prominent role TJs play in the formation of slip bands.

Still, questions remain concerning why certain TJs play a dominant role in producing intense slip bands. Which characteristics of TJ lines, when loaded, make them prone to forming slip bands? To address this, Charpagne et al. [10] studied the character of slip both close to and far away from TJs using a full-field crystal plasticity finite element (CPFE) model. The model predicted dominant activity of the experimentally observed localized slip system. Among the few TJs examined, slip activity was nearly single slip in the TJs with bands and multi-slip in TJs without slip bands. While insightful, since only a handful of TJs were modeled, the correlations had limited statistical significance. Why only a few TJs were sources for slip band formation remains to be clarified.

In this study, we combine 3D characterization and crystal plasticity modeling to analyze incipient slip band formation in thousands of triple junctions in the same lightly deformed Ni-based superalloy sample. To elucidate the propensity to trigger intense slip bands, the triple junctions without their observed slip bands are modeled within a large-scale representation of the experimental 3D microstructure, replicating, with high fidelity, the triple junction lines, grain boundaries and adjoining grains. The micromechanical response and slip activity near the TJs are compared with those near the boundaries and interiors of its parent grains. We find that TJs, on average, develop the largest concentrations of stress and grain-average re-orientation; however, among the TJs, there are no substantial differences in stress development. With statistical significance, the key differences between those bands observed to first produce slip bands lie in the development of grain-average re-orientation and their slip activity (including both the number of active slip systems and relative amounts of slip among the active ones). We show that TJs observed with slip bands tend to develop lower grain re-orientation and are more likely to operate *dominant single slip activity* than TJs observed with no slip bands. These distinctions strengthen with the amount of accumulated slip on the dominant slip system. Due to the large datasets examined here and rarity of slip band formation, a statistical analysis is performed to confirm that these differences are both statistically significant and substantive.

2. Materials and Methods

2.1. Materials

The material investigated is a precipitation strengthened polycrystalline nickel-base superalloy IN718 that displays a nominal composition of Ni - 0.56 %Al - 17.31%Fe - 0.14%Co - 17.97%Cr - 5.4%Nb - Ta-1.00%Ti - 0.023%C - 0.0062%N (wt%). The material was heat treated to produce large grain size and a high γ''-phase content. Thermal processing began with a solution annealing step, 30 min at 1050°C, followed by water quench. Afterwards, the material underwent precipitation hardening, which entails 8 h at 720°C followed by 8 h at 620°C. More details can be found elsewhere [7, 11].

2.2. Experimental Data Collection

Tensile testing was performed at room temperature using a custom in-situ 5000 N stage within a Thermo Fisher Scientific Versa3D Dual-Beam scanning electron microscope (SEM) on flat dog bone-shaped specimens with a gauge section of 1×3 mm^2. The test continued until a macroscopic strain of 1.83% where it was interrupted for high-resolution digital image correlation measurements. The speckle pattern used for these measurements was made by gold nanoparticle deposition with an average particle size of 60 nm [12]. To reduce imaging distortions, high magnification images were taken at horizontal field widths of 138 μm. To reduce drift distortions, large electron beam spot sizes and large dwell times (20 μs, 6 min per image) were used. In addition, to minimize charging effects and beam defect, low acceleration voltages of 5 kV and a external scan controller were employed [13, 14]. More details can be found elsewhere [7, 11, 15]. With the HR-DIC images collected during testing, the Heaviside-DIC method (H-DIC) was used to capture slip localization at the surface during deformation [16]. The Heaviside-DIC provide accurate location of slip events during deformation and quantitative measurement of the amplitude induced by slip [16]. The sample preparation, imaging conditions and Heaviside-DIC parameters allow for a discontinuity detection resolution between 0.2 and 0.3 pixels (7 nm and 10 nm respectively) [6, 16].

The TriBeam system [17] was used for the collection of orientation fields in 3D. After mechanical testing, the specimen was unloaded and 3D electron backscatter diffraction (EBSD) measurements performed. Electrical discharge machining cuts were performed to prepare a pillar with optimal geometry for a TriBeam experiment. The pillar is laser ablated with a slice thickness of 1 μm. Between each slice, EBSD measurements are collected with a step size of 1 μm to form cubic voxels. Backscatter electron (BSE) images were collected from the top surface of the pillar. BSE images were also collected every 30 slices for use with dataset stack alignment. A set of 526 slices was obtained during the experiment and reconstructed into a 3D dataset using the DREAM.3D software [18]. Prior to reconstruction, each EBSD slice was aligned to match the corresponding BSE image using the procedure described in [19].

Voxel-accurate alignment between HR-DIC and 3D EBSD data was carried out using the automated method described in [19], correcting the distortions in each slice of the 3D EBSD dataset. The procedure is presented in detail in [10] and consists in merging both EBSD and DIC data into a single file, extracting automatically all active slip planes using the local crystal orientation associated to every slip band, and reconstructing the slip bands in the first layer of grains after rotating their 3D normal in the sample reference frame. Each slip band consists in a one-voxel thick plane, defined by its normal and one point on the surface.

TJ voxels were identified per their 3D von Neumann neighborhood (i.e. immediate face neighbor voxels), as the voxels containing three distinct grain neighbors. Voxels joining the same grain triplets were flagged as belonging to the same TJ with each triplet of grain neighbors defining a unique TJ id number. Previous work had revealed peculiar configurations where slip bands emanate from some TJs [10]. To identify which TJs are in this configuration, the number of voxels shared by any TJ and any slip band in the dataset were calculated. If seven or more contiguous voxels were shared between a particular TJ and slip band, the TJ was flagged as triggering the formation of that slip band. A typical configuration of a TJ and intersecting slip band is presented in Figure 1. The experimental datasets (HR-DIC measurement, 3D voxelized dataset and 3D meshed dataset) are openly available on the Dryad TM data repository platform [20]. The related data descriptor article is available in the Scientific Data - Nature TM journal [21].

2.3. Computational Modeling Background

We begin by outlining the approach taken to build a full-3D experimentally informed microstructure authentic in the representation of the crystallography and grain structure morphology of the IN718 material. The creation of high-fidelity mesh representation of grains, boundaries and TJ lines was a critical step in this approach and is non-standard and hence will be detailed after a brief review of the constitutive law used.

Kinematics and Constitutive Law

The constitutive law used is the large strain formalism for elasticity and crystallographic slip developed by Kalidindi, Bronkhorst and Anand [22] and modified to model strain hardening via a dislocation density based hardening law. For IN718, the model considers plastic deformation to occur solely via dislocation slip on the 12 $\{111\}\langle 110\rangle$ FCC close-packed slip systems. The kinematics and constitutive laws defined in the model were introduced in the form of a user-defined mechanical material behavior (UMAT) subroutine implemented in ABAQUS/Standard.

Here, tensor and vector quantities are denoted by boldfaced uppercase and lowercase letters respectively. All other terms are scalars. Through multiplicative decomposition, the total deformation gradient tensor $\mathbf{F}$ can be separated into

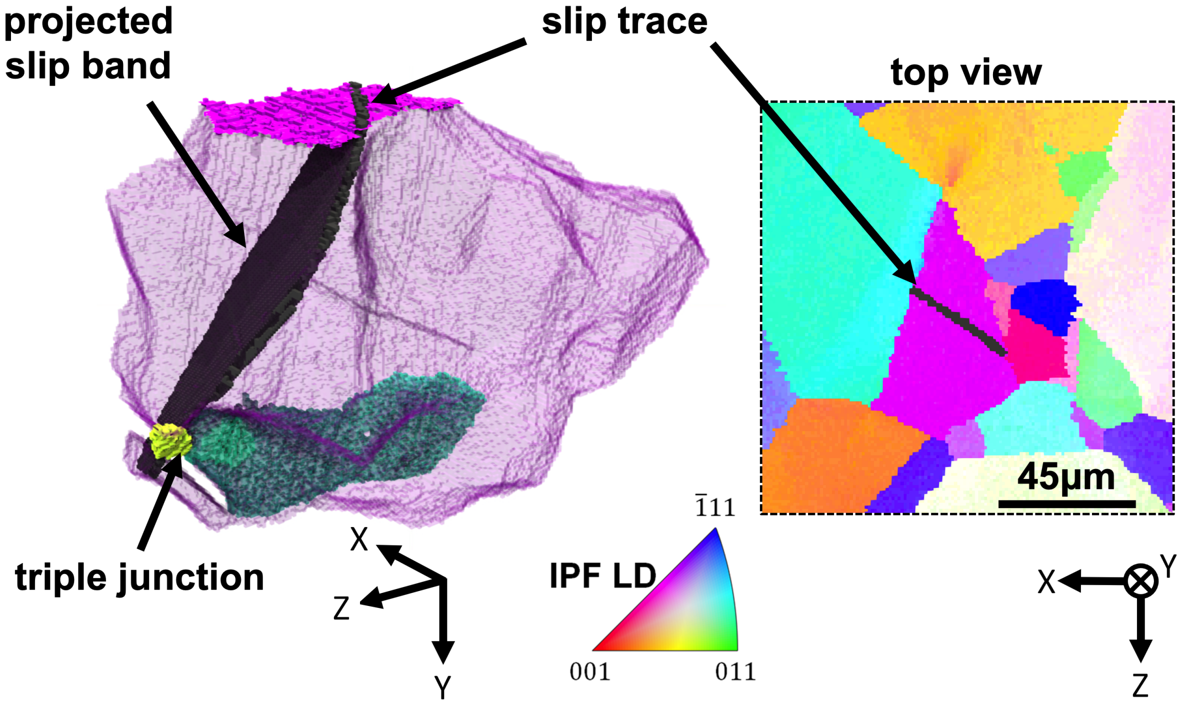

Fig. 1 A typical configuration of a slip band emanating from a triple junction line. A surface-visible slip trace is labeled in the experimental voxel dataset. With known slip plane geometry, the slip band is projected in 3D through the depth of the grain where it intersects along the triple junction line below. Voxels are colored according to the crystallographic orientation along the loading direction.

elastic, $\mathbf{F}^e$, and plastic, $\mathbf{F}^p$, deformation gradient tensors as, $\mathbf{F} = \mathbf{F}^e\mathbf{F}^p$. The second Piola-Kirchhoff (2nd-PK) stress $\mathbf{S}$ due to the elastic deformation gradient $\mathbf{F}^e$ is computed according to the generalized Hooke's law,

$$\mathbf{S} = \mathbb{C} : \mathbf{E}^e \tag{1}$$

where $\mathbb{C}$ represents the fourth-order elastic stiffness tensor of the material and $\mathbf{E}^e$ is the work-conjugate Green-Lagrange elastic strain tensor. This strain tensor is given by $\mathbf{E}^e = \frac{1}{2}\left(\mathbf{F}^{eT}\mathbf{F}^e - \mathbf{I}\right)$, where $\mathbf{F}^{eT}$ represents the matrix transpose of the elastic deformation gradient and $\mathbf{I}$ is the identity matrix. The 2nd-PK stress is related to the Cauchy stress $\boldsymbol{\sigma}$ via the following relation,

$$\boldsymbol{\sigma} = \frac{1}{\det(\mathbf{F}^e)}\mathbf{F}^e\mathbf{S}\mathbf{F}^{eT}. \tag{2}$$

From the 2nd-PK stress, the resolved shear stress τ^α driving plastic slip on slip system α is computed according to Schmid's law,

$$\tau^\alpha = \mathbf{S} : (\mathbf{m}^\alpha \otimes \mathbf{n}^\alpha) \tag{3}$$

where $\mathbf{m}^\alpha$ and $\mathbf{n}^\alpha$ are the unit vectors along the slip direction and slip plane normal respectively.

The activity of a slip system α is represented by its slip rate, $\dot{\gamma}^{\alpha}$, and is calculated using the associated resolved shear stress according to a rate-dependent power-law flow rule similar to that suggested by Peirce, Rice and Needleman [23]

$$\dot{\gamma}^{\alpha} = \dot{\gamma}_0 \left| \frac{\tau^{\alpha}}{g^{\alpha}} \right|^n \mathrm{sgn}\,(\tau^{\alpha}) \tag{4}$$

where $\dot{\gamma}_0$ represents the reference slip rate, g^{α} the slip resistance on system α, and n the power-law exponent. Slip resistance evolves according to a generalized tensor form of the classic Taylor relation suggested by Franciosi et al. [24] taking into account the average interaction strengths between slip systems, given in Equation 6

$$g^{\alpha} = g_0 + \mu b \sqrt{\sum_{\beta} a^{\alpha\beta} \rho^{\beta}} \tag{5}$$

where g_0 is the structure independent slip system strength, μ the shear modulus, b the value of the Burgers vector, $a^{\alpha\beta}$ a dislocation-interaction matrix, and ρ^{β} the dislocation density on system β. The shear modulus is given by

$$\mu = \sqrt{C_{44} \left(\frac{C_{11} - C_{12}}{2} \right)} \tag{6}$$

The dislocation densities for each system evolve according to the Kocks-Mecking equation (Equation 7) [25], composed of a positive storage rate term and a negative dynamic recovery term

$$\dot{\rho}^{\alpha} = \frac{1}{b} \left(\frac{1}{K} \sqrt{\sum_{\beta} a^{\alpha\beta} \rho^{\beta}} - 2 y_c \rho^{\alpha} \right) |\dot{\gamma}^{\alpha}| \tag{7}$$

where K is a constant that describes dislocation junction strength, and y_c is the critical annihilation distance. Table I lists the values of all constitutive model parameters. The model calibration process involves successfully replicating experimental stress-strain curves (see Figure 9 in Appendix) and has been detailed in previous studies [10, 15].

Microstructure Model and Boundary Conditions

A CPFE mesh for micromechanical calculations was created directly from a characterized 3D microstructure. The full microstructure, however, is a voxel-based dataset that is too highly resolved for one-to-one voxel to mesh element mapping. Conversion to a CPFE model then becomes influenced by two opposing factors: maximizing the number of sufficiently resolved, high fidelity TJs, while not exceeding a practical number of elements for computational efficiency. With the present computational capabilities, this limit was set to 5 million fully-integrated linear hexahedral elements (C3D8). Under these constraints, creating a mirrored microstructure down to its TJs involved two main steps: 1) coarsening the full voxelized data set and determining a subvolume from the characterized surface to be modeled and 2) converting the voxelized microstructure subvolume into an FE mesh.

Table I: Constitutive model parameters.

Parameter	Value	Unit
C_{11}	259.6	GPa
C_{12}	179	GPa
C_{44}	109.6	GPa
$\dot{\gamma}_0$	10^{-3}	s^{-1}
n	20	-
g_0	400	MPa
b	0.257	nm
$\alpha^{\alpha\beta}$	0.1	-
ρ_0	1.5×10^{12}	m^{-2}
K	10	-
y_c	2.57	nm

In the first step, the resolution of the dataset was reduced by a factor of two in each of the three axes (i.e., voxel size of 2μm). The lower portion of Figure 2(a) shows a typical grain under the coarsened grid. The grain remains highly resolved and retains the geometry of its respective grain boundaries and triple lines. Next, a subvolume from the characterized surface is selected. Of the two in-plane surface dimensions and third out-of-plane depth, the latter is of primary importance, since the subvolume should capture not only the TJ lines but all three of their adjoining grains. Figure 3(a) shows the histograms of the first and second layer surface grain depths. A subset depth of 75 voxels was found to span the entire first layer surface grains and 90% of the second layer. Not exceeding the element number limit of 5M corresponds to a subset dimension of $200 \times 75 \times 200$ voxels.

We then determined the location of a subvolume that maximized the number of *high-confidence* TJs. This label refers to the increased confidence placed in model predictions at particular TJs based on their representation in the CPFE model. High-confidence TJs are those whose entire line geometry and volume of their three constituent grains are fully enclosed by the model without cropping at the subset faces/edges. In this work, direct comparisons between model predictions and experimental observations of slip bands are reserved exclusively for high-confidence TJs. Candidate subsets from the reduced resolution microstructure were sampled laterally along both x and z-axes in a rasterized-fashion, with each time counting the number of high-confidence TJs. Figure 3b shows the final voxel subvolume.

The second step converts this voxelized microstructure subvolume into an FE mesh with the aim to preserve the complex 3D geometry of the TJ lines and their adjoining grains. The former refers to replicating the natural smoothness of the grain boundaries and triple lines and avoiding "stair-step" artifacts in the micromechanical fields

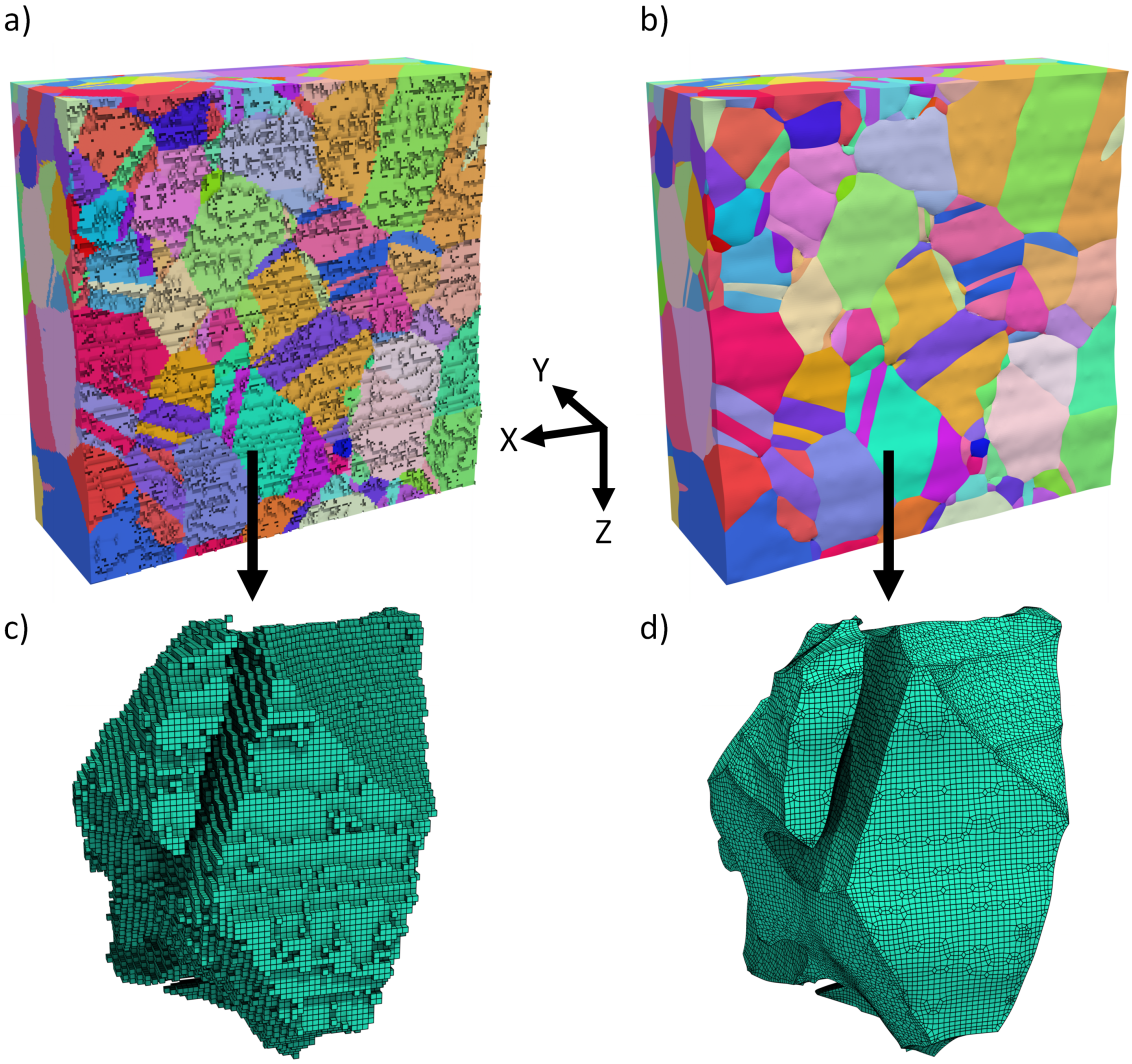

Fig. 2 Before-and-after visualization of the meshing procedure. (a) Selected subset of the reduced IN718 voxel dataset. (b) Final mesh model with smooth grain boundary surfaces. (c, d) Corresponding voxel and mesh representations of a selected grain. Voxels and mesh elements are colored according to the crystallographic orientation along the loading direction.

that would otherwise develop near non-conforming voxel mesh [26]. Preserving the morphology of the adjoining three grains is critical to recreating the local boundary conditions. To accomplish both, the finite element mesh is generated using Sculpt [27], a companion application to the Cubit Meshing and Geometry Toolkit developed at Sandia National Laboratories [28]. When the IN718 voxel subvolume subset is initially input into CUBIT, a pre-processing step is performed to remove small grains (containing fewer than five voxels), and repair certain voxel configurations at grain boundary interfaces which would result in non-manifold or poor quality mesh. Then, the grain boundaries and TJ lines are smoothed. Finally, an additional layer of hexahedral elements is inserted at the grain boundary interfaces to further improve smoothness and mesh quality at grain boundaries and TJs.

Figure 2(b) presents the final mesh consisting of 4.8 million elements of type C3D8. As a demonstration of the mesh's high fidelity, a comparison of before-and-after meshing is provided for a selected grain in Figure 2(c, d). As a quantitative test of fidelity, the percentage of microstructural features preserved post-meshing was analyzed with 95% of both grains and boundaries, as well as 90% of TJs being preserved as a fraction of their original count in the experimental subset. Additionally, the total grain volume, boundary area, and TJ length are preserved at rates of 99, 98, and 94% respectively. In total, the model contains 3665 TJs, 477 of which are considered high-confidence.

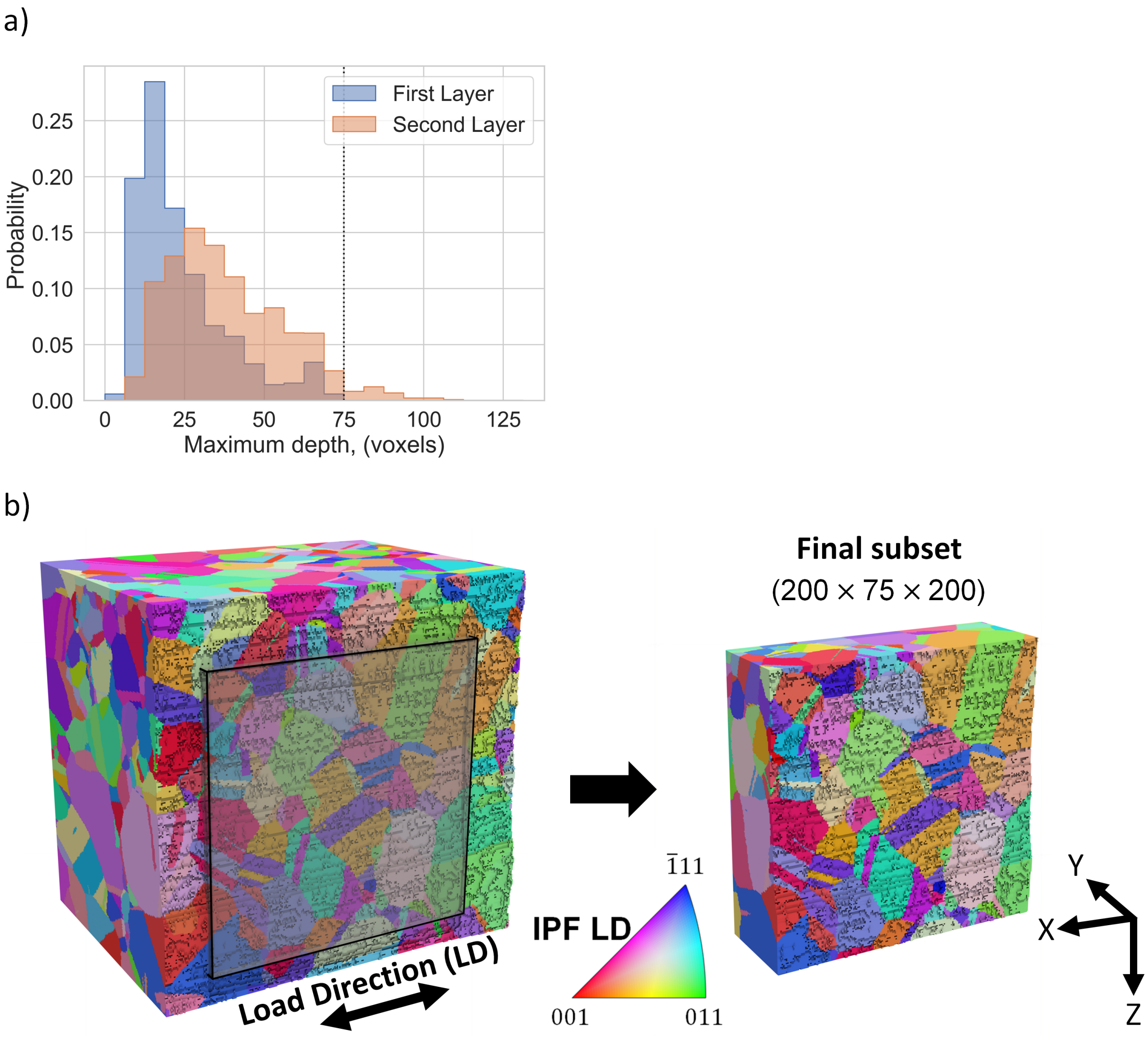

Fig. 3 (a) Histograms of first and second layer surface grain depths of the reduced IN718 voxel dataset. Dotted line indicates the selected subset depth. (b) Location and dimensions of the final subset selection. Grains colored according to the crystallographic orientation along the loading direction.

Next, crystallographic orientations were assigned to mesh elements. Elements belonging to the same grain were assigned the corresponding grain-average orientation from the TriBeam dataset. Although the dataset was obtained post-deformation, the grain-average misorientations were still sufficiently low, less than 1°.

To distinguish the behavior of grain interiors, grain boundaries, and TJs, the elements in the microstructure mesh are classified into these three distinct, mutually exclusive element sets: grain interiors, boundaries, and TJs. Each were defined according to the distance between element centroids and grain boundary or TJ interfaces. Elements whose centroids were located more than 5 microns away (3–4 element widths) from any grain boundary or TJ interface, were labeled as grain interior elements. Those whose centroids were located within 5 microns (3–4 element widths) from TJ lines were labeled as TJ elements, and any remaining elements were labeled as grain boundary elements. Figure 4 shows these three regions for the studied microstructure. The grain interior, grain boundary, and triple junction element sets comprise 1.9, 1.8 and 1.1 million elements respectively.

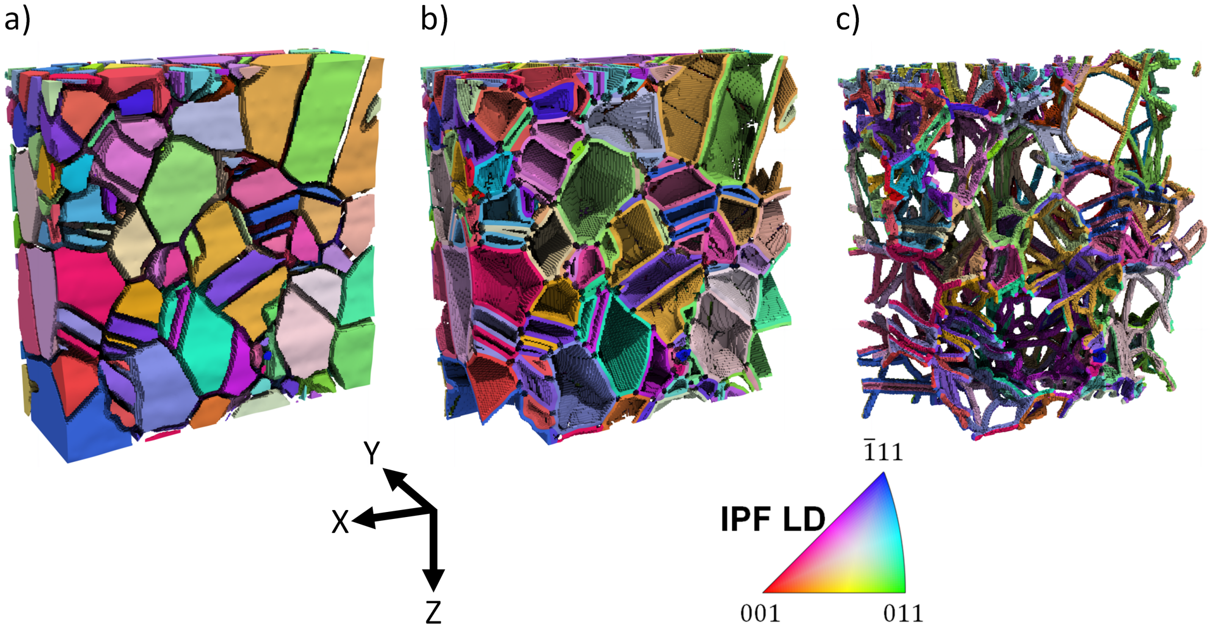

Fig. 4 Element sets of the IN718 CPFE model: (a) grain interiors, (b) grain boundaries, (c) all 3665 triple junctions. Mesh elements colored according to the crystallographic orientation along the loading direction.

In simulating deformation, displacement-controlled boundary conditions were applied to the model. Uniaxial monotonic tension was applied in the x-direction at a strain rate of $10^{-3}\mathrm{s}^{-1}$. All other faces of the virtual sample remained traction-free. With the exception of the experimental free surface, the traction-free boundary conditions of the lateral faces are inconsistent with experiment. Selection of high-confidence TJs also serves to limit any potential negative impact of the applied boundary conditions. With the goal of understanding incipient plasticity, the total final strain was 0.8%, corresponding to macroscopic yield at an offset strain of 0.2%. All analyses presented hereinafter are taken at 0.8% total strain.

3. Results

3.1. Triple Junctions Compared to Grain Boundaries and Interiors

With interest in those potential locations for slip band initiation, we compare in Figure 5 the von Mises equivalent stress, the cumulative slip on all slip systems, and grain reference orientation deviation (GROD) for the three distinct microstructure regions under 0.8% deformation. The von Mises stress σ_{VM} and cumulative slip γ are defined respectively as,

$$\sigma_{\mathrm{VM}} = \sqrt{\frac{(\sigma_{11} - \sigma_{22})^2 + (\sigma_{22} - \sigma_{33})^2 + (\sigma_{33} - \sigma_{11})^2 + 6(\sigma_{12}^2 + \sigma_{23}^2 + \sigma_{13}^2)}{2}} \tag{8}$$

$$\gamma = \sum_{\alpha=1}^{12} \int_0^t |\dot{\gamma}^{\alpha}| dt \tag{9}$$

and GROD is obtained from the following equation [29]:

$$\Delta\theta_{n,GROD} = \arccos\left(\frac{\mathrm{tr}(\mathbf{O}_n \widetilde{\mathbf{O}}^T) - 1}{2}\right) \tag{10}$$

where $\mathbf{O}_n$ represents the 3×3 orientation matrix of element n, and $\widetilde{\mathbf{O}}$ denotes the reference orientation of that element's respective grain. See Appendix for details of the GROD calculation.

In Figure 5(a), on average, the TJs experience the highest stress, followed by the grain boundaries, and last the grain interiors. This result is perhaps expected since, in general, achieving compatibility among three grains at a TJ is comparatively more difficult than at grain boundaries. The important differences lie at the high-stress range. There, regions near TJ experience significantly higher stress compared to grain interiors and even grain boundaries. This helps to explain why TJs would be preferred sites for slip band initiation over grain boundaries and grain interiors. When comparing in Figure 5(b) the cumulative slip among the different regions of microstructure, the only discernible difference was a slightly higher amount of cumulative slip for grain interiors compared to the other areas. The grain boundaries and TJs had almost identical cumulative slip. Regions near TJs do not on average develop larger plastic strains than elsewhere in the microstructure. Thus, perhaps non-intuitively, ease in plastic strain development is likely not a precursor event for slip band initiation.

Besides the total accumulation of slip, there are other ways in which these three microstructure features can differ in slip activity. One way is to compare the evolution of local lattice rotations, using the GROD. The GROD indicates how local regions of grain rotate differently with respect to the grain average. Here, the GROD is calculated for each element using the MTEX software [30] and the distributions of GROD within each microstructural class are examined. Figure 5(c) of the GROD distributions find that regions near TJs develop the largest GROD on average, followed by grain boundaries and then grain interiors with the least amount of GROD. Large values of GROD near TJs can also indicate that TJ slip activity diverges from that in the rest of the grain and even grain boundaries. This result, in conjunction with that of cumulative slip development, shows that while TJs are not associated with larger than

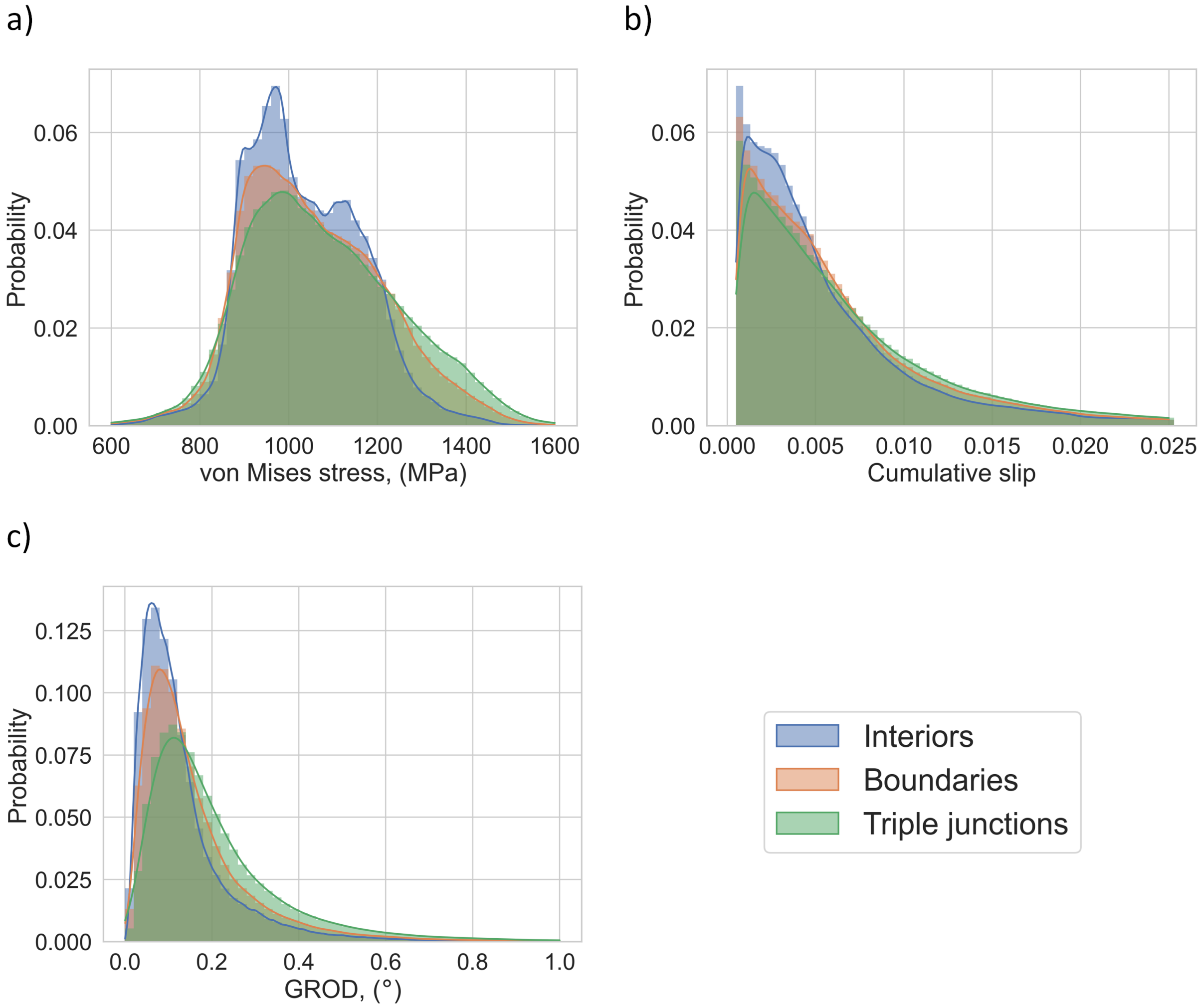

Fig. 5 Histograms of (a) von Mises stress, (b) cumulative slip, and (c) GROD for grain interior, boundary, and triple junction element sets.

average plastic strains, they do accommodate strain via different slip activity, either by slip on different slip systems than their adjoining grains or by slip on the same slip systems, but distributed differently, leading to larger amounts of slip re-orientations than the grain average.

3.2. Local micromechanics of triple junctions

We refine the scale of our analysis to compare one-to-one the TJs in the model and experimental microstructure. For this analysis, we only consider high-confidence TJs as defined earlier. This reduces the total number of TJs analyzed from 3665 to 477, 88 of which were observed to have slip bands emanating from their triple lines. Furthermore, for each TJ, we identify *subregions* of the TJ volume that belong to each grain. Accordingly, a TJ is comprised of three mutually distinct subregions (see Figure 6). For a subregion belonging to a surface-visible grain, it is possible to know whether a slip band emanated from it. Subregions are labeled as “Band” or “No-Band” accordingly. Slip bands cannot be detected in surface-invisible grains experimentally by DIC and thus subregions of a TJ belonging to these grains are not included in the Band/No-Band analysis. Here, TJ subregions are treated as individual entities. The element-wise average field values for each subregion are calculated and the distributions of these averages for "Band" and "No-Band" subregions inspected.

Figure 7(a) compares the von Mises stress in the TJ subregions with and without slip bands. No significant differences are found in the von Mises stress generated between Band and No-Band TJ subregions. While no distinction is found when considering all respective TJ subregions, it may be argued that only those which experience significant levels of plastic strain in the model are of interest. Figure 7(b) makes the same comparison exclusively among TJ subregions that accumulated an above average amount of slip on their primary active slip system, i.e., ($\gamma^{primary} > 5\times10^{-3}$). The result does not change; the von Mises stress level is similar between the Band/No Band TJs. Thus, while TJs may generate higher stress than grain boundaries and grain interiors, high stress is not the only pre-requisite for slip localization.

Figure 7(c) and (d) compare the GROD developed at these subregions. Slip band TJ subregions are associated with the lower GROD. The Band/No Band differences become more apparent when considering high-slip subregions. Earlier, we found that TJs are locations of high GROD compared to grain interiors and grain boundaries. When comparing among the grains belonging to the same TJ, the slip bands tend to form in the subregion with low GROD. This would suggest that the slip banding is favored in grains where the slip activity at the TJ is similar to that in the grain. Towards identifying the favorable slip activity for slip bands, we compare the number of active slip systems between the Band/No Band regions in Figure 7(e) and (f). Here a slip system is considered active if at 0.8% total strain its level of cumulative slip γ^{α} is greater than 10^{-4}. The model indicates smaller number of active slip systems within Band TJ subregions compared to No-Band subregions. This distinction increases further when considering high-slip subregions.

3.3. Slip activity indicators of slip band formation

To further investigate slip activity in the Band/No Band TJ subregions, we calculate the *slip dominance* and *slip ratio* to characterize the distribution of slip among the active slip systems. Both quantities are related to the average cumulative slip of each slip system for a given subregion. *Slip dominance* is defined as the maximum contribution of cumulative slip of any slip system to the overall cumulative slip. It ranges from $\frac{1}{12}$ to 1, indicating respectively cases where there is equal activation of all 12 slip systems, and cases where only one slip system was ever active. *Slip ratio* is the ratio of cumulative slip between the second-most and most active systems and ranges from 0 to 1. Simultaneously larger values of slip dominance and smaller values of slip ratio indicate predominant single slip. While these two metrics are not independent, they offer different insight into the distribution of slip activity. For instance it is possible for a grain to have both relatively high slip dominance and slip ratio, indicating predominance of two slip systems. Based on the earlier analysis, we posit that TJs prone to forming a slip band have both lower slip ratio and higher slip dominance compared to other TJs.

Figure 8 indicates that Band TJ subregions develop higher slip dominance and lower slip ratio compared to No-Band subregions. This is more pronounced for subregions that have developed significant levels of plastic slip. Both slip dominance and slip ratio are shown to be effective indicators of slip localization. The consistency between the calculations and experimental observations of slip band formation suggests that the incipient slip localization behavior of IN718, and potentially other nickel-base superalloys, is governed to a significant degree by the micromechanical interactions of grains. It is predominantly a result of a combination of TJ line geometry, the crystallographic orientations of the three adjoining grains, and their incompatibility in deformation when stressed.

4. Discussion

4.1. Rare microstructural conditions for slip band initiation

It has been theorized that grain boundaries and TJs are likely spots of intense slip band formation in nickel-base superalloys in part because these regions develop elevated incompatibility stresses due to large elastic anisotropy [10, 31, 32]. Experimental and computational studies of these alloys provide evidence of TJs developing complex stress states and activating multiple slip systems, some of which are locally unique compared to the predominantly single slip activated in corresponding grain centers [15]. Results of this analysis support this viewpoint, however much less is known with regard to what makes certain triple junctions over others prone to initiating slip bands. Our analysis demonstrates no significant differences in von Mises stress between the two types of TJ subregions, suggesting that while development of critically high stresses is important for slip in general in these regions, it does not play a decisive role in their incipient slip localization behavior.

Intrinsic and extrinsic defects associated with TJ lines and corresponding grain boundaries are also considered to be important factors in slip band initiation. In the absence of deformation, intrinsic defects at TJs result from orientation mismatch at the boundary junctions. Both grain boundary misorientations and TJ crystallography (i.e., grain boundary dihedral angles) have significant effects on the character of these defects and excess elastic strain energy produced at TJs [33–35]. Other extrinsic defects resulting from plastic incompatibility may exist at TJ lines before deformation as a product of thermo-mechanical history [35]. Both types of defects are believed to play a substantial role in slip activation near TJ lines, with particular focus drawn towards the character of adjoining grain boundaries and their effects. Slip system activation, development of persistent slip bands, and fatigue crack nucleation at TJs have all be found to depend highly on the number of coherent twin, and random grain boundaries they possess [10, 36, 37]. This dependence extends to the IN718 system where slip bands are found to emanate from TJs with at least one coherent twin boundary, more so than those that consist of three random boundaries [10]. Conventional crystal plasticity does not account for defect character of TJs and grain boundaries. Doing so requires additional treatment of dislocation/boundary interactions and non-local hardening. Still, the conventional CPFE model used here predicts significant differences in the relative distribution of slip between the TJ subregions based solely upon on geometry, crystallography and incompatibility driven by elastic anisotropy. These findings support the idea that slip band initiation along TJ lines is not simply dictated by their defect character and instead is controlled to a considerable degree by their inherent grain neighbor constraints and resultant distribution of slip activity.

The foregoing results suggest that usage of metrics, like slip dominance and slip ratio, would be valuable for advanced crystal plasticity model formulations that model slip bands explicitly. Many of such models implement local material softening as a means of triggering slip localization [38–40]. Some in particular invoke an exponential decay of critical resolved shear stress with increased slip rate or accumulated slip to achieve localization [41, 42]. Moving forward, metrics like slip dominance and slip ratio which account for the distribution of accumulated slip could be integrated into these advanced formulations in ways which could affect either threshold conditions and/or the evolution of strain softening. Optimal parameter configurations may then be set through grainscale calibrations with experiment.

4.2. Statistical significance

While noticeable differences in the calculated distributions of micromechanical quantities between Band and No-Band TJ subregions arise, these may be biased due to choice of binning and imbalance of classes. Of the 477 high-confidence, surface visible TJs, 117 are Band and 831 No-Band TJ subregions of which 59 and 365 are considered as high-slip subregions, respectively. With this level of class imbalance and the similarity of distribution shapes among most CPFE quantities analyzed, there is potential for any visible differences between histograms to be related to random sampling.

Given that most of the distributions presented are heavily skewed and non-normal, we opted for a non-parametric ("distribution-free") hypothesis test to assess stochastic equality of Band and No-Band TJ subregions. We performed two-tailed Mann–Whitney U-tests for all CPFE quantities discussed with the assumption that the samples tested were mutually independent [43, 44]. The Mann–Whitney U-test is conceptually similar to the well-known Student's t-test as it is used to check for significant differences between two independent groups with regard to a single variable [45]. However, whereas the t-test leverages assumptions of the distributions, including normality and equal variance, to evaluate shifts in sample means, the Mann–Whitney U-test evaluates for shifts in the main mass of probability between samples. The test operates by first combining observations from two samples (e.g., samples "1" and "2") and ranking them from one to N, where N represents the total sample size ($n_1 + n_2 = N$). A common choice of ranking is from lowest to highest value are smallest to largest. Once ranks are assigned, summed rank scores are computed for each sample (R_1 and R_2) and a U value is computed for each sample as,

$$U_1 = R_1 - \frac{n_1\,(n_1 + 1)}{2} \tag{11}$$

$$U_2 = R_2 - \frac{n_2\,(n_2 + 1)}{2} \tag{12}$$

The smaller of U_1 and U_2 is reported as the final U-statistic with smaller values indicating greater group separation (e.g., $U = 0$, complete separation). Lastly, U can be compared with critical values, $U_{critical}$, to determine statistical significance (P value). The hypotheses tested were the null hypothesis, H_0, being that the two samples (averaged CPFE quantities of Band and No-Band TJ subregions) are from the same distribution, and the alternative hypothesis, H_a, being that the distributions differ.

The U-test, like most statistical tests, may report statistically significant differences given large enough sample sizes even when the magnitude of those differences may be negligible. Therefore, along with null hypothesis testing, we compute Cliff's δ effect sizes to determine whether any reported differences between Band and No-Band subregions are substantive. Cliff's δ is a non-parametric effect size that quantifies the difference between two groups of observations and is calculated as,

$$\delta = \frac{{}^{\#}(X_1 > X_2) - {}^{\#}(X_1 < X_2)}{n_1 n_2} \tag{13}$$

where ${}^{\#}(X_1 > X_2)$ represents the number of values from group 1 greater than those of group 2, and ${}^{\#}(X_1 < X_2)$ represents the reverse case [46]. Values of δ range from -1 to $+1$, with extreme values indicating no intersection of the groups and a value of 0 indicating complete overlap.

Results of the statistical tests can be found in Table II. When considering all TJ subregions ($n_1 = 117$ and $n_2 = 831$), the U-tests report very significant differences ($P < 0.001$) between subregions with respect to slip dominance and slip ratio, each with non-negligible effect size. For the case of high-slip subregions ($n_1 = 59$ and $n_2 = 365$), very significant differences ($P < 0.001$) were found for all quantities besides von Mises stress with increased effect sizes in line with the observations made in Sections 3.2 and 3.3. By modeling a large number of TJs with high-fidelity microstructure representation and incorporation of experimental observation of slip bands, statistically significant evidence is found pointing to differences in local micromechanical response between TJs that do and do not produce slip bands.

5. Conclusions

Combined 3D characterization of slip bands and 3D high-fidelity micromechanical calculations on the same 3D microstructure are carried out to understand the microstructural triple junction (TJ) features that promote slip band initiation. Considering the multiple variables at play and their statistical variations, to establish relevant correlations, the analysis is performed on thousands of TJs. The TJs display unique deformation behavior compared to other features of the microstructure like grain interiors and boundaries. Additionally, the model predicts significant differences in local micromechanical response between TJs with and without experimentally observed slip bands emanating from their triple lines. The main conclusions are as follows:

1. TJs are likely sources of slip localization as they develop higher stresses on average compared to interior regions of grains and even grain boundaries.
2. Overall cumulative slip development between grain interiors, boundaries, and TJs is very similar and does not explain the proclivity of slip localization at TJs.

Table II: Results of the two-tailed Mann–Whitney U-tests for all TJ subregions and those with appreciable slip on the primary system, $\gamma^{primary} > 5 \times 10^{-3}$. Reported are test statistics, U, P values, and Cliff's $|\delta|$ effect size.

CPFE variable	$\gamma^{primary}$	U	P value	$\lvert\delta\rvert^{*}$
von Mises stress	-	44973	0.388	0.05
	$> 5 \times 10^{-3}$	11035	0.76	0.02
GROD	-	40754	0.02	0.14
	$> 5 \times 10^{-3}$	6936	1.15×10^{-5}	0.36
# Active systems	-	42532	0.08	0.10
	$> 5 \times 10^{-3}$	6393	5.49×10^{-7}	0.41
Slip dominance	-	56903	4.31×10^{-4}	0.20
	$> 5 \times 10^{-3}$	14450	2.49×10^{-5}	0.34
Slip ratio	-	39182	2.78×10^{-3}	0.17
	$> 5 \times 10^{-3}$	7298	7.12×10^{-5}	0.32

[*] Effect size interpretations: negligible ($|\delta| < 0.147$), small ($0.147 \geq |\delta| < 0.33$), medium ($0.33 \geq |\delta| < 0.474$), and large ($|\delta| \geq 0.474$) [47].

3. TJs experimentally observed to produce slip bands develop lower grain-average reorientation, and activate fewer slip systems compared to those without observed bands. The number of active slip systems at these TJs is mostly one and no more than two. Evidently, slip bands preferably form in a grain that has nearly single slip on the same slip system *both* at the TJ and in its entire volume.
4. On average, TJs with slip bands observed undergo more localized slip on one slip system than those without slip bands as measured via percentage of overall cumulative slip (slip dominance), and relative cumulative slips of the first and second-most active systems (slip ratio).
5. These differences in slip activity between band and no-band TJs are pronounced among those TJs that experience above-average cumulative slip.

Acknowledgments

This work is funded by the U.S. Dept. of Energy, Office of Basic Energy Sciences Program DE-SC0018901. Use was made of computational facilities purchased with funds from the National Science Foundation (CNS-1725797) and administered by the Center for Scientific Computing (CSC). The CSC is supported by the California NanoSystems Institute and the Materials Research Science and Engineering Center (MRSEC; NSF DMR 1720256) at UC Santa Barbara.

References

[1] D. V. V. Satyanarayana, N. Eswara Prasad, Nickel-Based Superalloys, in: N. E. Prasad, R. J. H. Wanhill (Eds.), Aerospace Materials and Material Technologies : Volume 1: Aerospace Materials, Springer Singapore, Singapore, 2017, pp. 199–228. doi:10.1007/978-981-10-2134-3_9.
URL https://doi.org/10.1007/978-981-10-2134-3{_}9

[2] J. C. Stinville, W. C. Lenthe, M. P. Echlin, P. G. Callahan, D. Texier, T. M. Pollock, Microstructural statistics for fatigue crack initiation in polycrystalline nickel-base superalloys, International Journal of Fracture 208 (1-2) (2017) 221–240. doi:10.1007/s10704-017-0241-z.

[3] M. I. Latypov, J.-C. Stinville, J. R. Mayeur, J. M. Hestroffer, T. M. Pollock, I. J. Beyerlein, Insight into microstructure-sensitive elastic strain concentrations from integrated computational modeling and digital image correlation, Scripta Materialia 192 (2021) 78–82. doi:https://doi.org/10.1016/j.scriptamat.2020.10.001.
URL http://www.sciencedirect.com/science/article/pii/S1359646220306448

[4] J. C. Stinville, E. Martin, M. Karadge, S. Ismonov, M. Soare, T. Hanlon, S. Sundaram, M. P. Echlin, P. G. Callahan, W. C. Lenthe, V. M. Miller, J. Miao, A. E. Wessman, R. Finlay, A. Loghin, J. Marte, T. M. Pollock, Fatigue deformation in a polycrystalline nickel base superalloy at intermediate and high temperature: Competing failure modes, Acta Mater. 152 (2018) 16–33. doi:10.1016/j.actamat.2018.03.035.

[5] J. Stinville, W. Lenthe, J. Miao, T. Pollock, A combined grain scale elastic–plastic criterion for identification of fatigue crack initiation sites in a twin containing polycrystalline nickel-base superalloy, Acta Materialia 103 (2016) 461–473. doi:https://doi.org/10.1016/j.actamat.2015.09.050.
URL https://www.sciencedirect.com/science/article/pii/S1359645415007399

[6] J. C. Stinville, P. G. Callahan, M. A. Charpagne, M. P. Echlin, V. Valle, T. M. Pollock, Direct measurements of slip irreversibility in a nickel-based superalloy using high resolution digital image correlation, Acta Mater. 186 (2020) 172–189. doi:10.1016/j.actamat.2019.12.009.

[7] M. Charpagne, J. Stinville, P. Callahan, D. Texier, Z. Chen, P. Villechaise, V. Valle, T. Pollock, Automated and quantitative analysis of plastic strain localization via multi-modal data recombination, Materials Characterization 163 (2020) 1–16.

[8] J. C. Stinville, M. A. Charpagne, A. Cervellon, S. Hemery, F. Wang, P. G. Callahan, V. Valle, T. M. Pollock, On the origins of fatigue strength in crystalline metallic materials, Science 377 (6610) (2022) 1065–1071. arXiv:https://www.science.org/doi/pdf/10.1126/science.abn0392, doi:10.1126/science.abn0392.
URL https://www.science.org/doi/abs/10.1126/science.abn0392

[9] R. Jiang, F. Pierron, S. Octaviani, P. Reed, Characterisation of strain localisation processes during fatigue crack initiation and early crack propagation by sem-dic in an advanced disc alloy, Materials Science and Engineering: A 699 (2017) 128 – 144. doi:http://dx.doi.org/10.1016/j.msea.2017.05.091.
URL http://www.sciencedirect.com/science/article/pii/S0921509317307074

[10] M. Charpagne, J. Hestroffer, A. Polonsky, M. Echlin, D. Texier, V. Valle, I. Beyerlein, T. Pollock, J. Stinville, Slip localization in inconel 718: A three-dimensional and statistical perspective, Acta Materialia 215 (2021) 117037. doi:https://doi.org/10.1016/j.actamat.2021.117037.
URL https://www.sciencedirect.com/science/article/pii/S1359645421004171

[11] J. Stinville, M. Charpagne, F. Bourdin, P. Callahan, Z. Chen, M. Echlin, D. Texier, J. Cormier, P. Villechaise, T. Pollock, V. Valle, Measurement of elastic and rotation fields during irreversible deformation using heaviside-digital image correlation, Materials Characterization (2020) 110600doi:https://doi.org/10.1016/j.matchar.2020.110600.
URL http://www.sciencedirect.com/science/article/pii/S1044580320320714

[12] A. D. Kammers, S. Daly, Self-assembled nanoparticle surface patterning for improved digital image correlation in a scanning electron microscope, Experimental Mechanics 53 (2013) 1333–1341.

[13] J. Stinville, M. Echlin, D. Texier, F. Bridier, P. Bocher, T. Pollock, Sub-grain scale digital image correlation by electron microscopy for

polycrystalline materials during elastic and plastic deformation, Experimental Mechanics (2015) 1–20`doi:10.1007/s11340-015-0083-4`.
URL `http://dx.doi.org/10.1007/s11340-015-0083-4`

[14] W. C. Lenthe, J.-C. Stinville, M. P. Echlin, Z. Chen, S. Daly, T. M. Pollock, M. De Graef, Custom scan control and time resolved signal acquisition for high resolution sem imaging, Microscopy and Microanalysis 24 (S1) (2018) 536–537. `doi:10.1017/S1431927618003173`.

[15] J. M. Hestroffer, M. I. Latypov, J.-C. Stinville, M.-A. Charpagne, V. Valle, M. P. Miller, T. M. Pollock, I. J. Beyerlein, Development of grain-scale slip activity and lattice rotation fields in inconel 718, Acta Materialia 226 (2022) 117627. `doi:https://doi.org/10.1016/j.actamat.2022.117627`.
URL `https://www.sciencedirect.com/science/article/pii/S1359645422000118`

[16] F. Bourdin, J. C. Stinville, M. P. Echlin, P. G. Callahan, W. C. Lenthe, C. J. Torbet, D. Texier, F. Bridier, J. Cormier, P. Villechaise, T. M. Pollock, V. Valle, Measurements of plastic localization by heaviside-digital image correlation, Acta Materialia 157 (2018) 307–325. `doi:10.1016/j.actamat.2018.07.013`.

[17] M. P. Echlin, M. Straw, S. Randolph, J. Filevich, T. M. Pollock, The tribeam system: Femtosecond laser ablation in situ sem, Materials Characterization 100 (2015) 1–12. `doi:https://doi.org/10.1016/j.matchar.2014.10.023`.
URL `https://www.sciencedirect.com/science/article/pii/S104458031400326X`

[18] M. A. Groeber, M. A. Jackson, DREAM.3d: A digital representation environment for the analysis of microstructure in 3d, Integrating Materials and Manufacturing Innovation 3 (1) (2014) 56–72. `doi:10.1186/2193-9772-3-5`.
URL `https://doi.org/10.1186/2193-9772-3-5`

[19] M.-A. Charpagne, F. Strub, T. M. Pollock, Accurate reconstruction of ebsd datasets by a multimodal data approach using an evolutionary algorithm, Materials Characterization 150 (2019) 184–198. `doi:https://doi.org/10.1016/j.matchar.2019.01.033`.
URL `https://www.sciencedirect.com/science/article/pii/S1044580318329073`

[20] Dryad data repository.
URL `https://datadryad.org/`

[21] J. C. Stinville, J. M. Hestroffer, M. A. Charpagne, A. T. Polonsky, M. P. Echlin, C. J. Torbet, V. Valle, K. E. Nygren, M. P. Miller, O. Klaas, A. Loghin, I. J. Beyerlein, T. M. Pollock, Multi-modal dataset of a polycrystalline metallic material: 3D microstructure and deformation fields, Scientific Data 9 (1) (2022) 460.

[22] S. Kalidindi, C. Bronkhorst, L. Anand, Crystallographic texture evolution in bulk deformation processing of FCC metals, Journal of the Mechanics and Physics of Solids 40 (3) (1992) 537–569. `doi:10.1016/0022-5096(92)80003-9`.
URL `https://www.sciencedirect.com/science/article/pii/0022509692800039`

[23] D. Peirce, R. Asaro, A. Needleman, Material rate dependence and localized deformation in crystalline solids, Acta Metallurgica 31 (12) (1983) 1951 – 1976. `doi:https://doi.org/10.1016/0001-6160(83)90014-7`.
URL `http://www.sciencedirect.com/science/article/pii/0001616083900147`

[24] P. Franciosi, M. Berveiller, A. Zaoui, Latent hardening in copper and aluminium single crystals, Acta Metallurgica 28 (3) (1980) 273 – 283. `doi:https://doi.org/10.1016/0001-6160(80)90162-5`.
URL `http://www.sciencedirect.com/science/article/pii/0001616080901625`

[25] H. Mecking, U. Kocks, Kinetics of flow and strain-hardening, Acta Metallurgica 29 (11) (1981) 1865–1875. `doi:https://doi.org/10.1016/0001-6160(81)90112-7`.
URL `http://www.sciencedirect.com/science/article/pii/0001616081901127`

[26] Y. Choi, M. Groeber, T. Turner, D. Dimiduk, C. Woodward, M. Uchic, T. Parthasarathy, A crystal-plasticity fem study on effects of simplified grain representation and mesh types on mesoscopic plasticity heterogeneities, Materials Science and Engineering: A 553 (2012) 37–44. `doi:https://doi.org/10.1016/j.msea.2012.05.089`.
URL `http://www.sciencedirect.com/science/article/pii/S0921509312007952`

[27] S. J. Owen, C. E. Ernst, C. J. Stimpson, Sculpt: Automatic parallel hexahedral mesh generation`doi:10.2172/1762652`.
URL `https://www.osti.gov/biblio/1762652`

[28] T. D. Blacker, S. J. Owen, M. L. Staten, W. R. Quadros, B. Hanks, B. W. Clark, R. J. Meyers, C. Ernst, K. Merkley, R. Morris, C. McBride, C. J. Stimpson, M. Plooster, S. Showman, Cubit geometry and mesh generation toolkit 15.1 user documentationdoi:10.2172/1430472.
URL https://www.osti.gov/biblio/1430472

[29] A. Morawiec, Orientations and rotations, Springer, 2003.

[30] F. Bachmann, R. Hielscher, H. Schaeben, Texture analysis with mtex–free and open source software toolbox, Solid State Phenomena 160. doi:10.4028/www.scientific.net/SSP.160.63.

[31] X. Song, Y. Wang, J. Zhang, Y. Lu, Y. Wang, Z. Chen, The formation of intragranular stress concentration in plastic deformed ni-base superalloy: Governing factors and process, Materials Science and Engineering: A 806 (2021) 140820. doi:10.1016/j.msea.2021.140820.
URL https://doi.org/10.1016/j.msea.2021.140820

[32] L. Sang, J. Lu, J. Wang, R. Ullah, X. Sun, Y. Zhang, Z. Zhang, In-situ SEM study of temperature-dependent tensile behavior of inconel 718 superalloy, Journal of Materials Science 56 (28) (2021) 16097–16112. doi:10.1007/s10853-021-06256-8.
URL https://doi.org/10.1007/s10853-021-06256-8

[33] P. Fortier, G. Palumbo, G. Bruce, W. Miller, K. Aust, Triple line energy determination by scanning tunneling microscopy, Scripta metallurgica et materialia 25 (1) (1991) 177–182.

[34] M. Upadhyay, L. Capolungo, V. Taupin, C. Fressengeas, Grain boundary and triple junction energies in crystalline media: A disclination based approach, International Journal of Solids and Structures 48 (22) (2011) 3176–3193. doi:https://doi.org/10.1016/j.ijsolstr.2011.07.009.
URL https://www.sciencedirect.com/science/article/pii/S0020768311002563

[35] L. Priester, The triple junction, in: Grain Boundaries, Springer series in materials science, Springer Netherlands, Dordrecht, 2013, pp. 305–336.

[36] M. Li, D. J. Duquette, Y. Chen, Deformation accommodation at triple junctions in columnar-grained nickel, Metallurgical and Materials Transactions A 50 (1) (2018) 52–57. doi:10.1007/s11661-018-4998-0.
URL https://doi.org/10.1007/s11661-018-4998-0

[37] S. Kobayashi, T. Inomata, H. Kobayashi, S. Tsurekawa, T. Watanabe, Effects of grain boundary- and triple junction-character on intergranular fatigue crack nucleation in polycrystalline aluminum, Journal of Materials Science 43 (11) (2008) 3792–3799. doi:10.1007/s10853-007-2236-z.
URL https://doi.org/10.1007/s10853-007-2236-z

[38] S. Forest, Modeling slip, kink and shear banding in classical and generalized single crystal plasticity, Acta Materialia 46 (9) (1998) 3265–3281. doi:10.1016/s1359-6454(98)00012-3.
URL https://doi.org/10.1016/s1359-6454(98)00012-3

[39] T. Erinosho, F. Dunne, Strain localization and failure in irradiated zircaloy with crystal plasticity, International Journal of Plasticity 71 (2015) 170–194. doi:https://doi.org/10.1016/j.ijplas.2015.05.008.
URL https://www.sciencedirect.com/science/article/pii/S0749641915000789

[40] X. Xiao, D. Song, J. Xue, H. Chu, H. Duan, A size-dependent tensorial plasticity model for FCC single crystal with irradiation, International Journal of Plasticity 65 (2015) 152–167. doi:10.1016/j.ijplas.2014.09.004.
URL https://doi.org/10.1016/j.ijplas.2014.09.004

[41] A. Marano, L. Gélébart, S. Forest, Intragranular localization induced by softening crystal plasticity: Analysis of slip and kink bands localization modes from high resolution FFT-simulations results, Acta Materialia 175 (2019) 262–275. doi:10.1016/j.actamat.2019.06.010.
URL https://doi.org/10.1016/j.actamat.2019.06.010

[42] B. Ahmadikia, M. A. Kumar, I. J. Beyerlein, Effect of neighboring grain orientation on strain localization in slip bands in HCP materials, International Journal of Plasticity 144 (2021) 103026. doi:10.1016/j.ijplas.2021.103026.
URL https://doi.org/10.1016/j.ijplas.2021.103026

[43] H. B. Mann, D. R. Whitney, On a Test of Whether one of Two Random Variables is Stochastically Larger than the Other, The Annals of Mathematical Statistics 18 (1) (1947) 50 – 60. `doi:10.1214/aoms/1177730491`.
URL `https://doi.org/10.1214/aoms/1177730491`

[44] P. E. McKnight, J. Najab, Mann-Whitney U Test, John Wiley Sons, Ltd, 2010, pp. 1–1. `arXiv:https://onlinelibrary.wiley.com/doi/pdf/10.1002/9780470479216.corpsy0524`, `doi:https://doi.org/10.1002/9780470479216.corpsy0524`.
URL `https://onlinelibrary.wiley.com/doi/abs/10.1002/9780470479216.corpsy0524`

[45] Student, The probable error of a mean, Biometrika 6 (1) (1908) 1–25.
URL `http://www.jstor.org/stable/2331554`

[46] N. Cliff, Dominance statistics: Ordinal analyses to answer ordinal questions., Psychological Bulletin 114 (1993) 494–509.

[47] J. Romano, J. Kromrey, J. Coraggio, J. Skowronek, Appropriate statistics for ordinal level data: Should we really be using t-test and Cohen's d for evaluating group differences on the NSSE and other surveys?, in: Annual meeting of the Florida Association of Institutional Research, 2006, pp. 1–3.

6. Appendix

6.1. Inconel 718 Stress-Strain Curves

6.2. Calculation of GROD

For a grain comprised of N elements with each element n having and orientation matrix $\mathbf{O}_n$, the average orientation matrix of the grain $\overline{\mathbf{O}}$ is calculated as

$$\overline{\mathbf{O}} = \frac{1}{N} \sum_{n=1}^{N} \mathbf{O}_n \tag{14}$$

The reference orientation of the grain $\widetilde{\mathbf{O}}$ is computed as the orientation which minimizes its averaged misorientation [29]. By defining a quantity $\mathbf{L}^2 = \overline{\mathbf{O}}^T \overline{\mathbf{O}}$, $\widetilde{\mathbf{O}}$ is specified by the relation

$$\widetilde{\mathbf{O}} = \mathbf{L} \overline{\mathbf{O}}^{-1} \tag{15}$$

making the final calculation of GROD for an element n expressed as

$$\Delta\theta_{n,GROD} = \arccos\left(\frac{\mathrm{tr}(\mathbf{O}_n \widetilde{\mathbf{O}}^T) - 1}{2} \right). \tag{16}$$

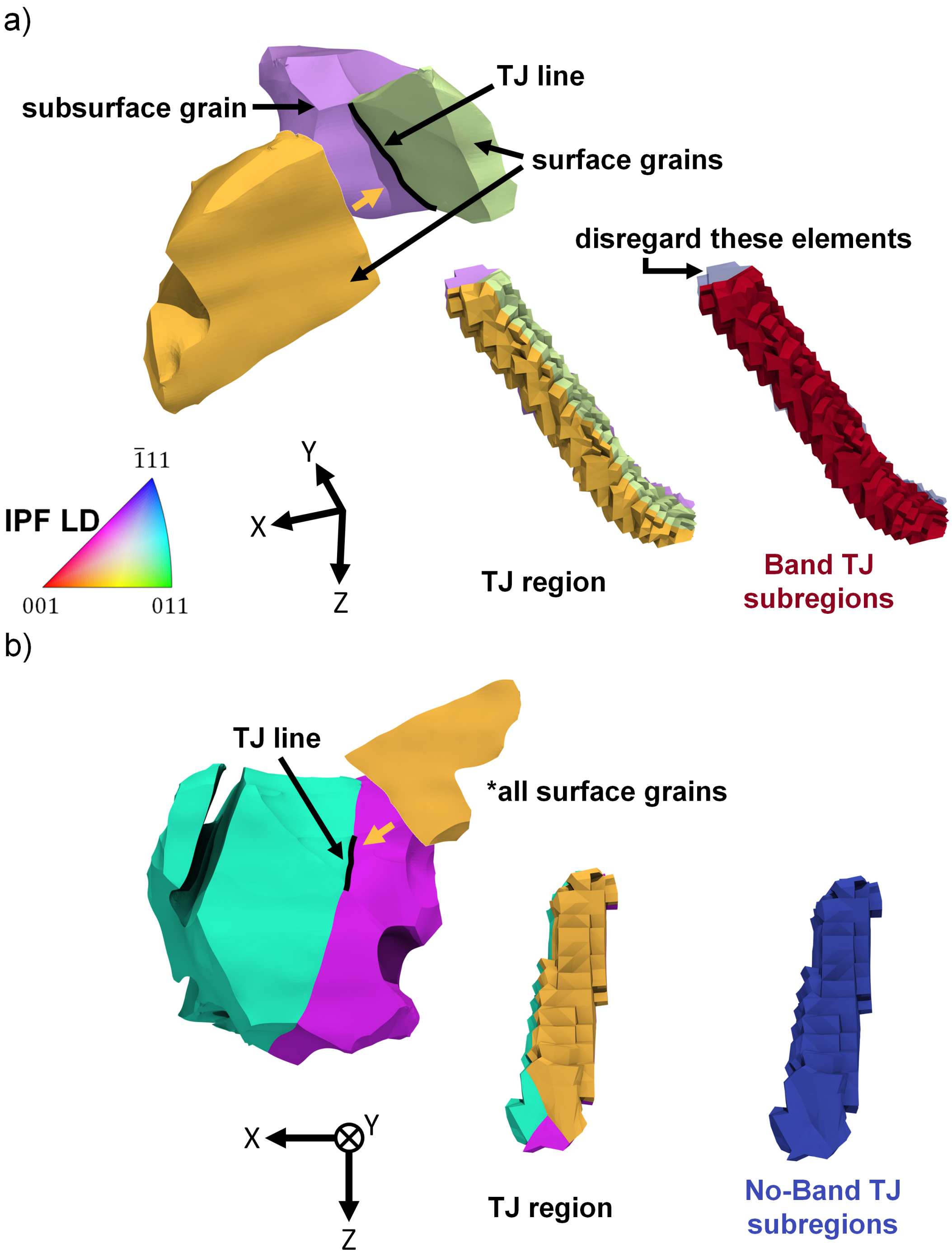

Fig. 6 Visual illustration of the “Band” and “No-Band” element labelling approach. (a) Example triple junction (TJ) consisting of two surface-visible grains, each of which had a band emanating from the TJ line. Elements belonging to the surface-invisible grain are discarded. (b) Example TJ where all three grains are surface-visible, yet no slip band is found emanating from the TJ line in any grain. Mesh elements colored according to the crystallographic orientation along the loading direction. Band and No-Band subregion elements colored red and blue separately.

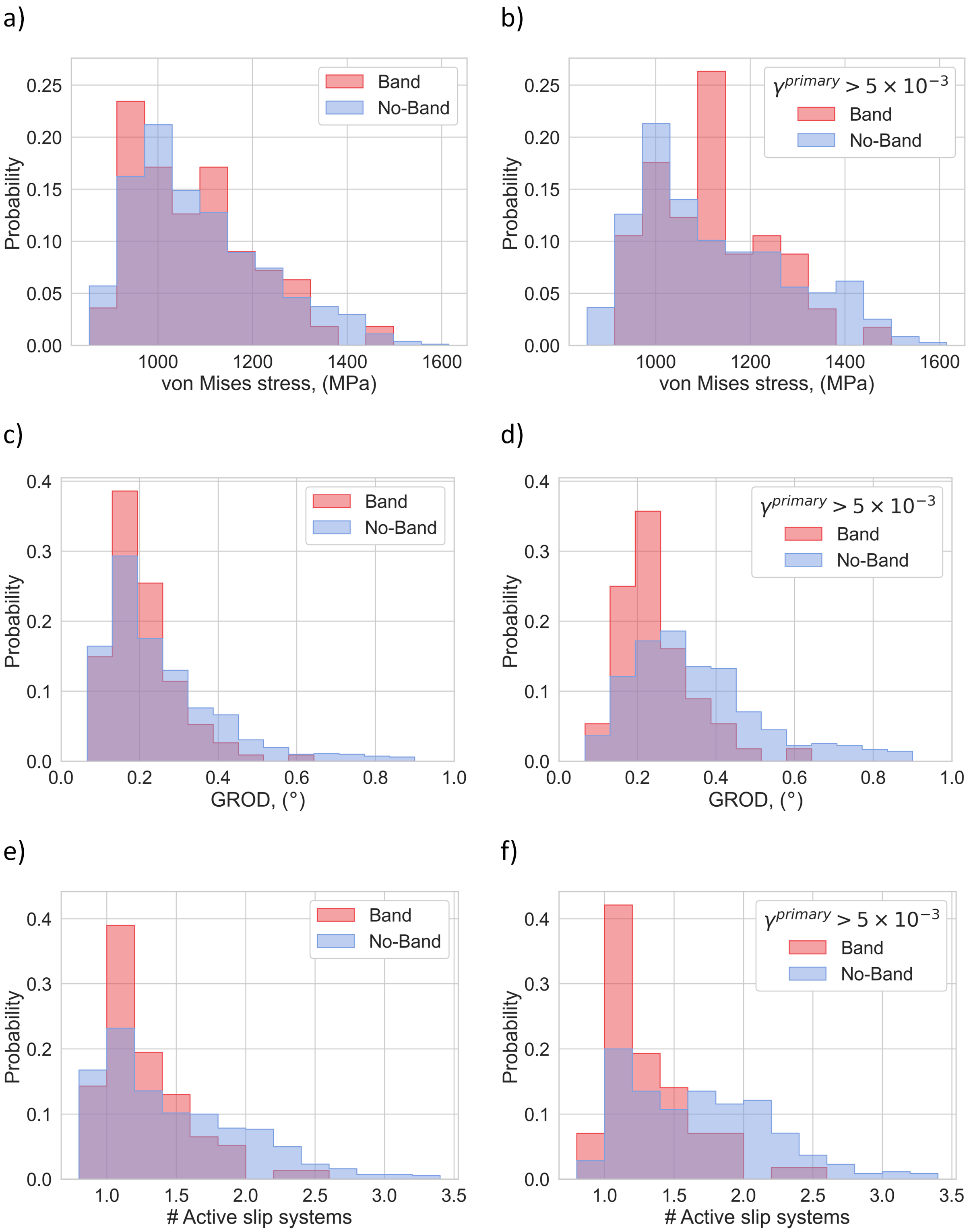

Fig. 7 Histograms of von Mises stress, GROD, and number of active slip systems for (a, c, e) all Band and No-Band TJ subregions and (b, d, f) TJ subregions with above-average cumulative slip on their primary system, $\gamma^{primary} > 5 \times 10^{-3}$. Histograms are semi-transparent, regions of purple indicate overlap.

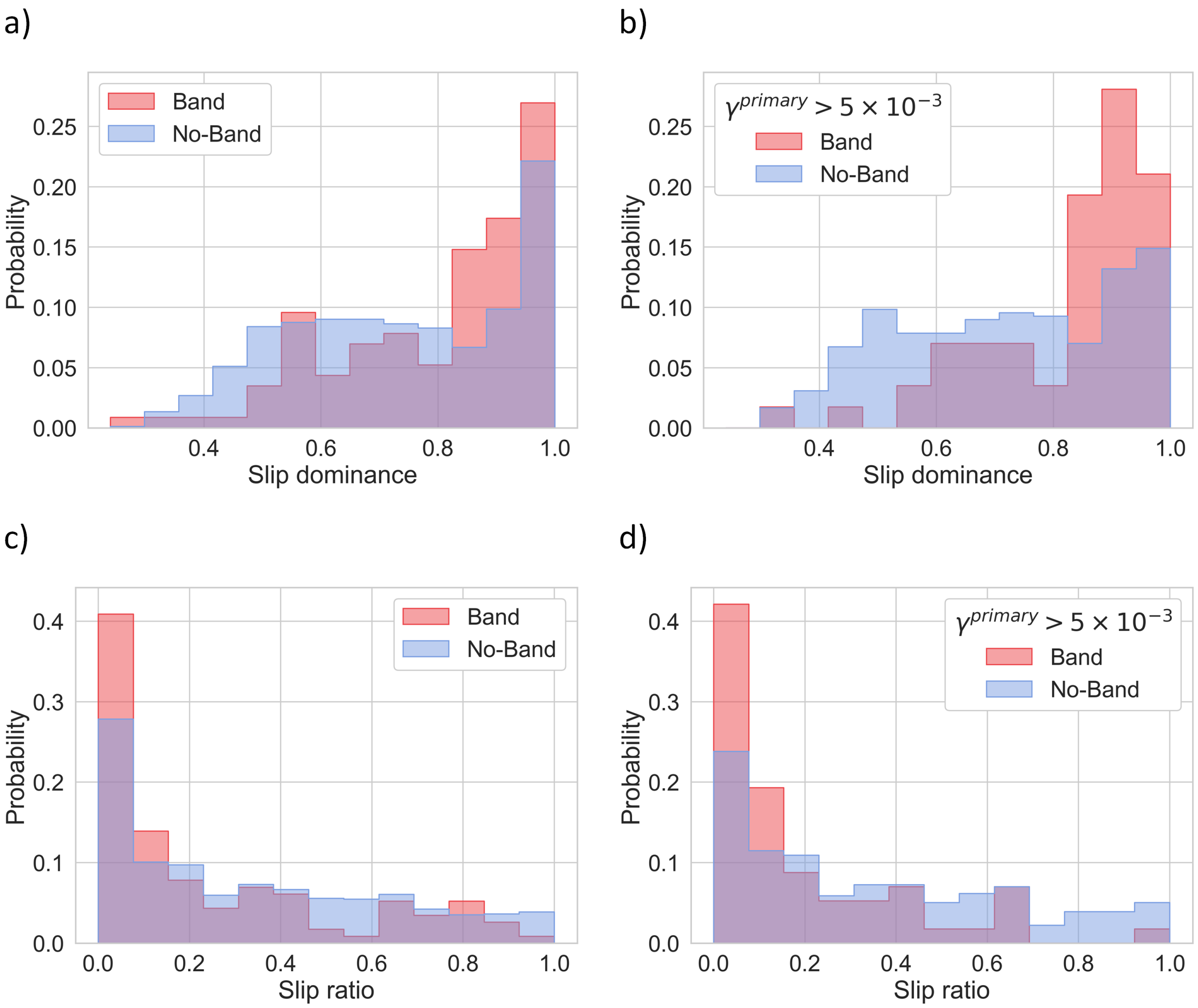

Fig. 8 Histograms of slip dominance and slip ratio for (a, c) all Band and No-Band TJ subregions and (b, d) TJ subregions with above-average cumulative slip on their primary system, $\gamma^{primary} > 5 \times 10^{-3}$. Histograms are semi-transparent, regions of purple indicate overlap.

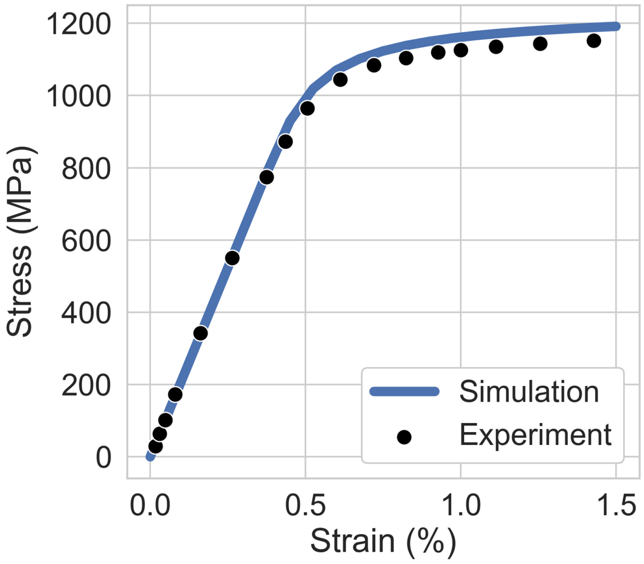

Fig. 9 Engineering stress-strain curves of IN718 measured by experiment and from the calibrated CPFE model. The calibration procedure has been detailed in previous studies [10, 15].